ACS APPLIED MATERIALS & INTERFACES

www.acsami.org

Research Article

CO_2 to Formic Acid Using Cu−Sn on Laser-Induced Graphene

Muqing Ren,[⊥] Hongzhi Zheng,[⊥] Jincheng Lei,[⊥] Jibo Zhang, Xiaojun Wang, Boris I. Yakobson,* Yan Yao,* and James M. Tour*

Cite This: *ACS Appl. Mater. Interfaces* 2020, 12, 41223−41229

Read Online

ACCESS | Metrics & More | Article Recommendations | Supporting Information

ABSTRACT: Converting CO_2 into fuels and other value-added chemicals *via* an electrochemical reduction method has recently attracted great interest. However, there are still challenges to find suitable catalysts with high selectivity toward the formic acid formation. Here, we report the bimetallic CuSn-based catalyst to reduce CO_2 to formic acid by optimizing the ratio of Cu to Sn to achieve the optimal selectivity. The catalyst is generated on laser-induced graphene. Among the catalysts, CuSn-4 with Cu/Sn atomic ratio close to 1:2 shows a faradaic efficiency of 99% toward formic acid with a high partial current density of 26 mA/cm^2. Density functional theory calculations demonstrate that OCHO* intermediate formation is more favorable than that of COOH* on Sn sites, while OCHO* intermediate formation is moderate on Cu sites. The synergetic catalytic effect between Cu and Sn would further favor HCOOH formation. This study provides significant insight into the mechanism of formic acid formation.

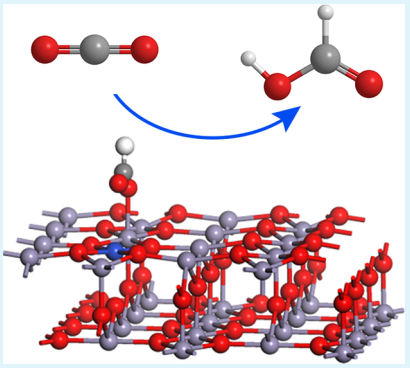

KEYWORDS: *laser-induced graphene, CuSn−LIG, electrochemical reduction, formic acid, carbon dioxide*

INTRODUCTION

Conversion of CO_2 into fuels and valuable chemical feedstocks is highly attractive since it provides a method to close the carbon cycle. Generally, the electrochemical reduction reaction of CO_2 (termed CO_2RR) could convert CO_2 to hydrocarbons and fuels including CH_4, CH_3OH, HCHO, HOOCCOOH, HCOOH, and CO.[1−3] Theoretically, the reduction of CO_2 to CO and HCOOH is advantageous over the other products due to the two-electron transfer pathway with relatively low thermodynamic barriers (−0.109 and −0.199 V *vs* RHE, respectively).[4−7] However, the reactions often involve multiple electron transfers that suffer from sluggish reaction kinetics and high thermodynamic overpotentials due to the adsorption configuration of the intermediates.[8,9] Currently, many catalysts have been screened to achieve high activity and selectivity in CO_2RR. Noble metal-based catalysts such as Pd, Au, Pt, and Ag are highly active and selective toward the reduction of CO_2 to CO, while Cd, Pb, Sn, and In-derived catalysts show remarkably high selectivity in the hydrogenation of CO_2 to formic acid.[10−16] Due to the large storage and safety requirements for CO during carbon sequestration and storage (CCS), the production of liquid formic acid is becoming a more attractive solution. Formic acid could be directly used as a feedstock for fuel cells and as a precursor for manufacturing value-added chemicals such as formate esters, methanol, and other carboxylic acids and derivatives.

Currently, the main challenge in formic acid production remains the high overpotential that greatly lowers the energy efficiency. The earth-abundant element Cu has gained intense interest due to its versatility in producing CO, HCOOH, and other hydrocarbons; however, the considerably high activity in the hydrogen evolution reaction (HER, the competing reaction against CO_2RR under cathodic conditions) and large overpotentials for CO_2 reduction of Cu catalysts have limited its practical applications. Consequently, optimizing Cu properties toward a lower potential and higher selectivity in CO_2RR is essential. Practical methods have been carried out to target this goal, such as surface improvement of Cu by cupric oxides, modification of Cu substrates with other metal elements, and by electroreduction assisted by photon irradiation or wet chemistry processes.[17−25] For instance, Kanan et al. modified polycrystalline Cu foil with a shell layer of Cu_2O through annealing and electrochemical reduction. It was found that the CO_2 reduction to HCOOH activity depends heavily on the thickness of Cu_2O, whereupon the highest faradaic efficiency (FE) of 33% was achieved.[26] Takanabe et al. made Cu−In alloy *via* thermal oxidation and electrochemical reduction. The alloy reached its highest activity in converting CO_2 to CO with a 90% FE at −0.5 V *vs* RHE.[27] Ye et al. developed a TiO_2−Cu_2O heterostructure to efficiently convert CO_2 to CH_4 photo-electrochemically.[28]

In this study, the earth-abundant element Sn was selected to enhance the properties of Cu in CO_2 reduction through a

Received: May 15, 2020
Accepted: August 24, 2020
Published: August 24, 2020

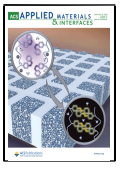

synergistic effect. While Sn catalysts usually suffer from a high overpotential in CO_2 reduction, their remarkably high selectivity attracted our attention. Several studies have been focused on the synergistic effect between Cu and Sn in high yields using Cu−Sn metallic alloy catalysts, and the combined metals strategy has proven to be effective in CO_2RR with high selectivity. This knowledge has been incorporated into the heterostructured catalysts. For example, Sun et al. modified the surface of Cu nanoparticles with a thin layer of SnO_2; the catalysts reached its highest activity in converting CO_2 to CO with a 93% FE at −0.7 V *vs* RHE.[19] The bimetallic copper oxides−tin (OD−Cu−Sn) that was synthesized through electrodeposition of Sn on an oxidized Cu sheet achieved more than 90% FE for CO at −0.6 V *vs* RHE, while the highest FE for the oxidized copper sheet alone was only ∼63%.[29] In addition to the Cu−SnO_2 oxides, Cu−Sn metallic alloy catalysts have demonstrated high selectivity toward formic acid production. The synthesized $Cu_{55}Sn_{45}$ alloy showed 89.5% FE for $HCOO^-$ at −1.09 V *vs* RHE.[30] Nevertheless, the solid-solution bimetallic oxides have been rarely studied. The presence of neighboring bimetallic sites in catalysts can modulate the surface adsorption of CO_2RR intermediates and improve the selectivity of certain species over the other ones, which result in a higher selectivity of the products.

To improve the FE, while lowering the overpotential and increasing the stability, we studied the synergistic effect of a series of CuSn−laser-induced graphene (LIG) catalysts in reducing CO_2 to formic acid with a high yield through tuning the ratios of Cu and Sn. LIG is a three-dimensional (3D) porous carbon material obtained through CO_2 laser writing on polyimide (PI). LIG possesses large porous structure, promotes the homogeneous distribution of active sites, and enhances the conductivity.[31−35] The CuSn−LIG catalysts were easily prepared based on seven different Cu/Sn molar ratios of the precursor solutions, 100:0 for CuSn-1, 80:20 for CuSn-2, 60:40 for CuSn-3, 50:50 for CuSn-4, 30:70 for CuSn-5, 15:85 for CuSn-6, and 0:100 for CuSn-7 (Supporting Information). The different ratios of Cu to Sn species alter the catalytic activity and selectivity of the bimetallic nanoparticles. The synergistic effect of Cu and Sn produces a highly selective formation of formic acid with up to ∼99% FE (at −1.0 V *vs* RHE), while either Sn alone or Cu alone can only generate formic acid or hydrogen with relatively low FEs, respectively. Density functional theory (DFT) calculations were conducted to evaluate the adsorption free energy of various intermediates on the catalyst surfaces. The combination of experimental and theoretical methods has demonstrated the synergistic effect between Cu and Sn, rendering the high selectivity for CO_2RR to $HCOO^-$. These findings may contribute to the design of high-performance catalysts, and could serve as a harbinger for future large-scale CO_2RR reduction to formic acid.

Preparation of a series CuSn−LIG catalysts was done through a re-lasing method as previously reported (Figure 1a).[28−32] PI was lased to make LIG, then exposed to an oxygen plasma to increase the hydrophilicity. The mixture solutions with different molar ratios ($CuCl_2$/$SnCl_2$) were dripped as aqueous solutions atop the oxidized LIG film and then the LIG was re-lased under the same conditions. The CuSn−LIG was then scraped from the PI surface to afford the active catalytic material. The representative highly efficient CuSn−LIG catalysts were characterized through transmission electron microscopy (TEM). As shown in Figure 1, the nanoparticles are homogeneously embedded in the LIG-based few-layer

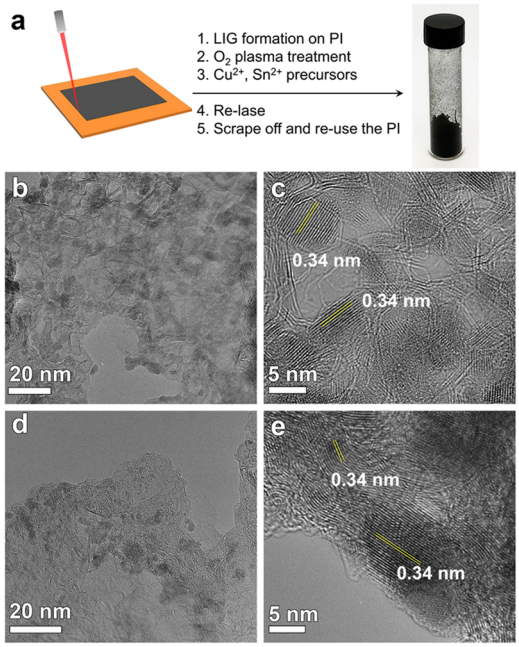

Figure 1. (a) Preparation of the CuSn−LIG catalysts. High-resolution TEM images of (b, c) CuSn-3 and (d, e) CuSn-4 catalysts.

graphene (evidenced by the distorted layered structure with a lattice spacing of ∼0.34 nm) as for CuSn-3 and CuSn-4 catalysts. The average sizes of the nanoparticles are ∼10 to 15 nm. The high-resolution TEM (HRTEM) images show the fine lattice structure of the nanoparticles. The *d*-spacing of 0.34 nm is in accordance with the (110) plane of SnO_2, suggesting that SnO_2 may be the primary phase in the catalysts. The *d*-spacings 0.20 and 0.26 nm (Figure S1) correspond to the (130) and (002) faces of $Cu(OH)_2$, respectively. The interfaces between $Cu(OH)_2$ and SnO_2 are observed in the CuSn-4 catalyst. The scanning TEM (STEM) mapping images (Figures S2 and S3) demonstrate the overlapping distribution of the metal species in bimetallic oxides, suggesting the hybrid structure of Cu−Sn oxide nanoparticles.

The oxidation state of Cu and Sn in CuSn-3 and CuSn-4 catalysts was analyzed by X-ray photoelectron spectroscopy (XPS). An XPS survey spectrum of CuSn-3, CuSn-4, and other ratios of CuSn catalysts demonstrates characteristic C, O, Cu, and Sn species (Figures 2 and S4−S6). As shown in Figure 2a, where the composition of Cu species is revealed, Cu $2p_{3/2}$ and Cu $2p_{1/2}$ spin-orbit binding energy are located at 932.7 and 952.8 eV, respectively. In addition, the presence of the shake-up peak at 942.8 eV further suggests the existence of Cu(II). Figure 2b shows the high-resolution Sn 3d region. The Sn species are mainly in the Sn(IV) state at 487 eV with a splitting of 8.5 eV for the Sn $3d_{3/2}$ component. The crystal structure of $Cu(OH)_2$ and SnO_2 was observed from the X-ray diffraction (XRD) pattern, which is consistent with the XPS result, confirming $Cu(OH)_2$ and SnO_2 were the two main forms in the CuSn-3 and CuSn-4 catalysts. Inductively coupled plasma optical emission spectrometry (ICP-OES) was employed in combination with XPS to determine the Cu/Sn ratios (Table S1). The atomic ratios of Cu/Sn in CuSn-3 and CuSn-4 are 0.049:0.046 and 0.038:0.077, respectively. Detailed discussion on the atomic ratios' variance is displayed in Table S1. Raman spectra (Figures 2d and S7) show the graphitic structure of the LIG-based catalysts. The clearly identified D, G, and 2D peaks

https://dx.doi.org/10.1021/acsami.0c08964
ACS Appl. Mater. Interfaces 2020, 12, 41223−41229

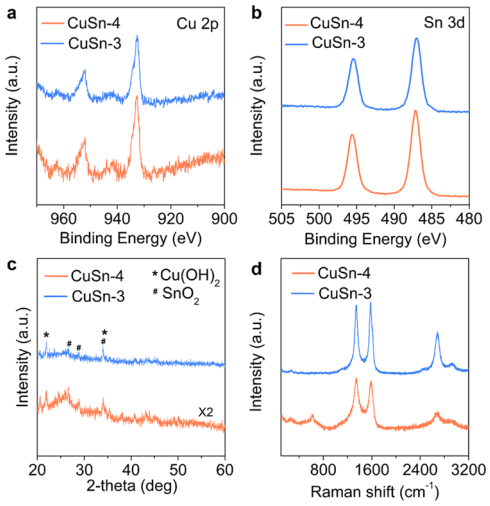

Figure 2. Structural and compositional characterizations of the catalysts. The high-resolution XPS spectra of CuSn-3 and CuSn-4 catalysts in the (a) Cu 2p and (b) Sn 3d regions. (c) Powder XRD pattern and (d) Raman spectra of CuSn-3 and CuSn-4 catalysts.

suggest the existence of multilayer graphene containing bent graphene layers in the foam structure,[36] or LIG, which is consistent with the TEM observations. The CuSn-4 catalyst shows an active mode located at 617 cm^{-1} that can be attributed to the expansion of the A_{1g} mode of Sn−O bonds. This further confirms the SnO_2 formation. The signal intensity of A_{1g} mode is very weak in the CuSn-3 catalyst. This phenomenon can be explained by the higher atomic ratio of Sn in CuSn-4 catalysts (Cu/Sn = 0.038:0.077), while the atomic ratio of Cu to Sn is equal to 1 in CuSn-3 catalysts (Cu/Sn = 0.049:0.046). The signal of the Sn−O expansion mode could be largely diminished.

A series of CuSn−LIG catalysts for CO_2RR electrochemical performance were tested through a Nafion-separated two-compartment H-cell. The electrolyte was CO_2-saturated 0.5 M $KHCO_3$ (pH ∼ 7.2). As shown in Figure 3, the current density

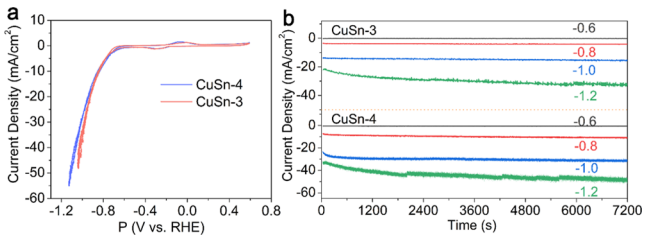

Figure 3. (a) Cyclic voltammograms curves of CuSn-3 and CuSn-4 in CO_2-saturated 0.5 M $KHCO_3$ solution, scan rate = 20 mV/s. (b) Chronoamperometric measurements of CuSn-3 and CuSn-4 in CO_2-saturated 0.5 M $KHCO_3$ solution.

of CuSn-3 was ∼48 mA/cm^2 at −1.03 V. The current density of CuSn-4 was ∼55 mA/cm^2 at −1.13 V. Both CuSn-3 and CuSn-4 have shown anodic and cathodic peaks between −0.4 and 0.2 V (Figure S8). CuSn-4 displayed a main anodic peak at −0.08 V (0.35 V *vs* SHE), corresponding to SnO/Sn being oxidized to SnO_2, and a shoulder peak at −0.01 V corresponding to Cu being oxidized to Cu(II). CuSn-3 displayed the main characteristic anodic peak at −0.01 V, while the intensity of the peak at −0.08 V decreased. This could be attributed to the lower content of Sn in CuSn-3 than CuSn-4, resulting in a lower anodic current density. CuSn-4 has two cathodic peaks at −0.21 and −0.28 V, respectively.[37] The peak at −0.21 V is due to Cu(II) being reduced to Cu and the peak at −0.28 V (0.15 V *vs* SHE) corresponds to the reduction of SnO_2 to SnO. The cathodic peaks of CuSn-3 shift toward higher potential by 0.03 V, which could also be caused by the increased Sn content.[38] Chronoamperometry tests were carried out to explore the stability of the catalysts and FE of products HCOOH and H_2 as illustrated in Figure 3b. Though the applied potentials varied from −0.6 to −1.2 V *vs* RHE, both CuSn-3 and CuSn-4 demonstrate relatively stable current densities, suggesting the high stability of the catalysts. For the CuSn-4 catalyst, the stable current density was ∼ −45 mA/cm^2 at an applied potential of −1.2 V. Chronoamperometry performance of the rest of the series of CuSn catalysts are shown in Figure S9. The products at different potentials were further analyzed and quantified by gas chromatography-mass spectrometry (GC-MS) and NMR (Figures S10 and S11).

The major CO_2RR products of CuSn catalysts are C1 products, including $HCOO^-$ (the stable form of formic acid in alkaline electrolytes) and CO, as well as hydrogen from HER. The LIG scaffold has very limited hydrogen evolution activity, which suppresses HER at high overpotentials.[39] The FE of $HCOO^-$ is shown in Figure 4a. The hybrid CuSn catalysts

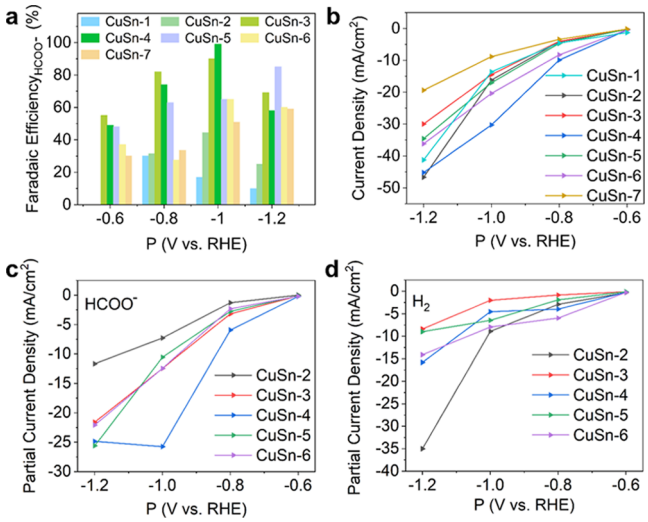

Figure 4. CO_2RR performance of the catalysts. (a) FE toward $HCOO^-$ based on a series of CuSn catalysts. (b) Current densities of CuSn catalysts are derived from chronoamperometric measurements. (c, d) Partial current densities toward (c) $HCOO^-$ and (d) H_2 derived from the chronoamperometric measurements. The chronoamperometric measurements for (b−d) are presented in Figures 3 and S9, and the current densities are calculated based on the geometric surface area of the electrode.

(CuSn-2 to CuSn-6) show higher $HCOO^-$ FEs than CuSn-1 (Cu only) and CuSn-7 (Sn only), which demonstrates the synergistic effect between Cu and Sn species. At −0.8 V *vs* RHE, CuSn-3 displays an 82% $HCOO^-$ yield. At −1.0 V *vs* RHE, both CuSn-3 and CuSn-4 demonstrated the optimal $HCOO^-$ formation performance, where the FEs are 90 and 99%, respectively. Meanwhile, the H_2 FE was largely suppressed (Figure S12), though not zero. The total FE may deviate from 100% for several reasons, especially when the FE is calculated from the partial efficiency based on different measuring techniques, which leads to the accumulation of

https://dx.doi.org/10.1021/acsami.0c08964
ACS Appl. Mater. Interfaces 2020, 12, 41223−41229

system error. The FE of HCOOH was calculated on the yield from the NMR analysis, while the H_2 FE was calculated from GC-MS analysis, two different instrumental techniques. The yield of formate is calculated from the NMR spectra with an internal standard; therefore, a high accuracy is expected. The deviation may originate from the efficiency of H_2 in that the very low yield of H_2 leads to errors during the measurements.

The nonunity FE is also widely observed in CO_2 reduction research. For example, Jaramillo et al. reported on the Sn electrode being applied for CO_2 reduction; the total FE varied from 90 to 110%.[40] Ohta et al. also observed that the total FE of CO_2 reduction was more than 100% due to the analytical instrument error.[41] Jin et al. used Au nanoclusters on CO_2 reduction to CO and H_2, in which total FE was ~102 ± 6%.[42] Therefore, although the total FE exceeds 100%, a high accuracy in determining the yield of formate has persisted.

The $HCOO^-$ formation efficiency at −1.0 V *vs* RHE order is: CuSn-4 > CuSn-3 > CuSn-5,6 > CuSn-7 > CuSn-2 > CuSn-1. The $HCOO^-$ FE was observed to be highly dependent on the ratios between Cu and Sn, and the highest $HCOO^-$ FE was obtained when the atomic percent of Sn is twice that of Cu (Table S1, CuSn-4, Cu_{atomic} 0.038:Sn_{atomic} 0.077). The weight percent of Cu and Sn in CuSn-4 are 4.8 and 18.4%, respectively. The weight percent of Cu and Sn in CuSn-3 are 6.7 and 12.0%, respectively (Table S1). This observed phenomenon is in accordance with previous research that the appropriate amount of Sn could enhance $HCOO^-$ selectivity. According to a previous study, the thickness of SnO_2 in Cu−SnO_2 core−shell nanoparticles could tune the selectivity toward $HCOO^-$ or CO. When the SnO_2 shell reached 1.8 nm, the $HCOO^-$ FE could rise to 85%; however, when the thickness was reduced to 0.8 nm, CO was the predominant product.[19] Huang et al. also reported that the presence of SnO_2 could promote the reduction of CO_2 to $HCOO^-$ and suppress the H_2 production in CuSn alloy nanowires.[43] One of the most plausible explanations proposed that $HCOO^-$ formation could occur on various metal surfaces through the OCHO* (* refers to a catalytic site where species is adsorbed) intermediate formed by the proton-coupled electron transfer (PCET) process. In this way, CO_2 is adsorbed as formate (OCHO*, eqs 1 and 2). However, depending on the protonation of the O or C atom, a competing intermediate COOH* is also generated.[20,44,45] The product of CO_2RR is highly dependent on the adsorption of intermediates on the catalytic sites. For example, CO and H_2O are generated from the COOH* with the progression of the reduction reaction, whereas OCHO* leads to the formation of formic acid. A recent study by Jaramillo et al. proposed a volcano plot to evaluate the ability and selectivity of various metal surfaces (Sn, Cu, Ag) in binding COOH* and OCHO* intermediates. The calculated result shows that Sn has an optimal binding energy with OCHO* intermediates while a weak binding to COOH* intermediates, which suggests that Sn has a high selectivity toward HCOOH formation.[40]

$$* + CO_2 + H^+ + e^- \rightarrow OCHO* \quad (1)$$

$$OCHO* + H^+ + e^- \rightarrow HCOOH + * \quad (2)$$

The total current densities in Figure 4b were calculated based on the geometric surface area of the catalysts. Partial current densities were calculated from the total current density (Figures 4b and S9) and corresponding FE (Figure 4a). At −1.2 V *vs* RHE, CuSn-4 demonstrates a total current density of 45 mA/cm^2 while the $HCOO^-$ current density reaches ~25 mA/cm^2. Meanwhile, at −1.0 V *vs* RHE, CuSn-4 shows a 30 mA/cm^2 total current density and 26 mA/cm^2 $HCOO^-$ current density. Though $HCOO^-$ current density of CuSn-3 is not as high as CuSn-4 at −1.0 V *vs* RHE, which is 12.4 mA/cm^2, it contributes most of the total current density (20.2 mA/cm^2) and leads to a high FE. These catalysts have shown excellent activity in CO_2 reduction to $HCOO^-$ activity as the feed Sn content varied from ~20 to ~100%. The CuSn-4 catalyst is among the best electrocatalysts in reducing CO_2 to $HCOO^-$ in terms of FE, partial current density, and overpotential (Table S2). Though the atomic ratios of CuSn-3 and CuSn-4 are quite similar, the concentration of the active sites may not be the same. A more abundant and uniform exposure of active sites at the surface of the nanoparticles could contribute to the improved activity of CuSn-4, in spite of the bulk concentration of the species. The valence states of Cu and Sn species after CO_2 reductions were also characterized by XPS. The valence state of Cu still maintains the Cu(II) state, while Sn maintains the Sn(IV) state. This illustrates the stability of CuSn−LIG catalysts.

To understand the synergetic effects of Cu and Sn in influencing the selectivity toward HCOOH, density functional theory (DFT) calculations were carried out to identify the rate-limiting steps (Figures 5, S13, S14, S15, Table S3, and S4). The metal species may experience redox at the overpotentials

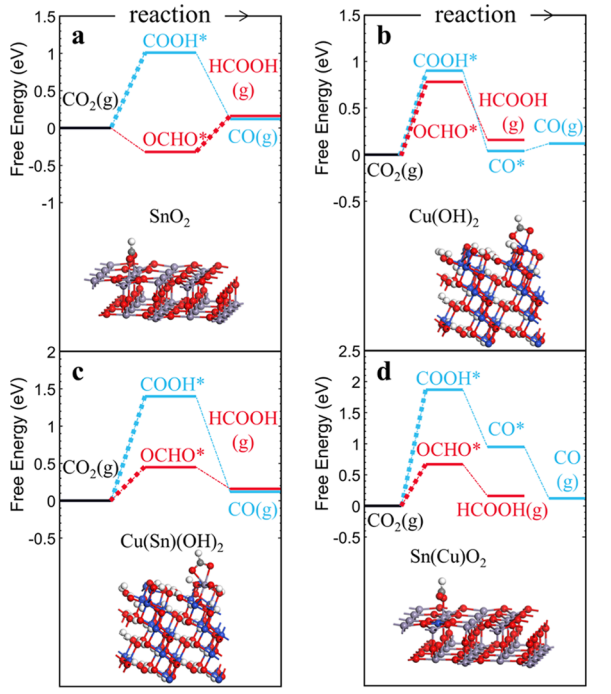

Figure 5. DFT simulation results. Free energy diagrams for the two competing reactions on (a) SnO_2 (110) surface, (b) $Cu(OH)_2$ (110) surface, (c) $Cu(Sn)(OH)_2$ surface ($Cu(OH)_2$ with one surface Cu substituted by the Sn atom), and (d) $Sn(Cu)O_2$ surface (SnO_2 with one surface Sn substituted by the Cu atom). Note that CO is physiosorbed on SnO_2 and $Cu(Sn)(OH)_2$, so the energy of CO* is not included for SnO_2 and $Cu(Sn)(OH)_2$. The rate-limiting steps are highlighted with square dots. Insets are the optimized structures of OCHO* adsorbed on the corresponding surface active sites (see Supporting Information Figure S13 for the configurations of other intermediates). Light purple, red, blue, white, and gray balls represent Sn, O, Cu, H, and C atoms, respectively.

https://dx.doi.org/10.1021/acsami.0c08964
ACS Appl. Mater. Interfaces 2020, 12, 41223−41229

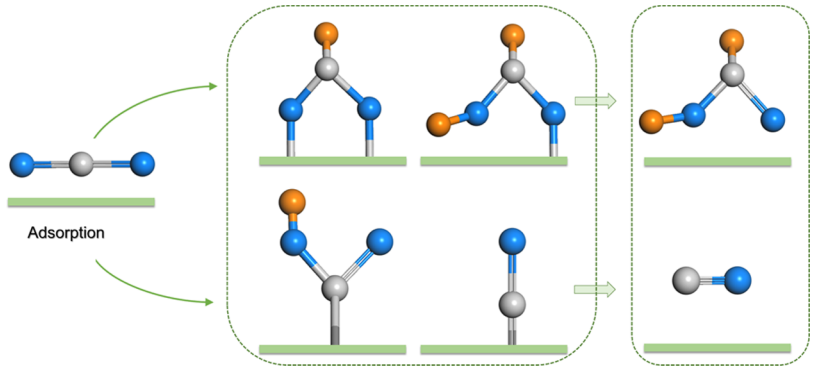

Figure 6. Mechanism for CO_2 reduction on CuSn catalysts includes two pathways toward HCOOH and CO production (gray spheres represent carbon; blue spheres represent oxygen; and orange spheres represent hydrogen).

lower than those for CO_2RR, which makes it very difficult to identify the valence state of the metal species from the *in-operando* catalysts. Additionally, in a catalytic cycle, the valence state of the site itself may also change (such as electron transfer) as the reaction proceeds, leading to even more complexity. The generally used approach is to generate free energy diagrams from DFT to evaluate the absorption of the reaction intermediates on the active sites. The structures for DFT are derived from the experimental TEM and XRD results (SnO_2 and $Cu(OH)_2$), and doping of Cu or Sn is evaluated. XPS results show that the valence states remain mostly unchanged after the electrochemical reactions. Instead of putting forward a tentative structure, we selected the Cu−SnO_2 and Sn−$Cu(OH)_2$ structures for the DFT. A similar treatment of the mix-ion structure has been proposed in other Cu-based catalysts.[19] Herein, HCOOH was considered as the final product to describe this reaction instead of formate, in line with the previously reported DFT calculations.[40,46,47] On the SnO_2 surface, the rate-limiting potential (Supporting Information) through COOH* and OCHO* intermediates are −1.01 and −0.48 V, respectively. It requires a much more negative potential to form CO through COOH* intermediate. Therefore, HCOOH is expected to be the major product. On $Cu(OH)_2$ surface, the free energy difference between COOH* and OCHO* is very small, ∼0.12 eV, suggesting both HCOOH and CO could be the products although HCOOH is still the preferred one. In the presence of the Sn atom on the surface of $Cu(OH)_2$, the rate-limiting potential of producing HCOOH through OCHO* intermediates could be largely decreased to −0.45 V, making HCOOH even more favorable. Therefore, the incorporation of Sn on a $Cu(OH)_2$ surface could significantly promote HCOOH formation. When substituting one surface Sn atom with Cu on the SnO_2 surface, the rate-limiting step of forming HCOOH changes from OCHO* → HCOOH to CO_2 → OCHO*. Although the rate-limiting potential slightly increases (−0.67 *vs* −0.48 V), it is still much lower than forming CO through the COOH* intermediate (−1.87 and −1.01 V with and without Cu substitution, respectively). The simulation results are in accordance with the experimental results. Among the series of CuSn−LIG catalysts, CuSn-4 has the highest HCOOH selectivity. At −1.0 V *vs* RHE, CuSn-4 demonstrated 99% FE_{HCOOH}. In CuSn-4 catalysts, the atomic ratio of Cu to Sn is 1:2. At −1.0 V *vs* RHE, CuSn-3 showed 90% FE_{HCOOH}; the atomic ratio of Cu to Sn is close to 1:1. However, CuSn-7 (Sn only) just showed ∼50% FE_{HCOOH} at −1.0 V *vs* RHE. Therefore, the synergetic effects of Cu and Sn lower the overpotential of the OCHO* intermediate and enhance the HCOOH selectivity.

Based on the experimental and theoretical analysis, the mechanism of CO_2 reduction on CuSn catalysts is proposed in Figure 6. The PCET can first take place through carbon or oxygen atoms binding to the electrode surface, which will result in COOH* or OCHO*, respectively. Carbon bonded COOH* is the key intermediate for CO production, while OCHO* is the key intermediate for HCOOH production. At −1.0 V *vs* RHE, CuSn-4 demonstrated 99% FE_{HCOOH}. In CuSn-4 catalysts, the atomic ratio of Cu to Sn is 1:2. According to the simulation result and the previous study at −0.9 V *vs* RHE, OCHO* binds more strongly with Sn than COOH* and steers Sn selectivity toward HCOOH; Cu has a weaker binding ability toward OCHO*. Based on the Sabatier principle, to achieve the highest activity, the catalysts should not bind too strongly or weakly with the reaction intermediates. Therefore, the synergetic effects of Cu and Sn result in CuSn-4, showing a superior activity toward HCOOH formation.

CONCLUSIONS

In this study, we demonstrated a very simple formation method to convert mixed composition nanoparticles into conductive graphene foams using LIG and a facile re-lasing method. This generates a series of highly efficient CuSn catalysts for the conversion of CO_2 to formic acid. The various ratios of Cu to Sn were investigated to understand the correlation between Cu−Sn ratios and the selectivity toward formic acid. CuSn-4 catalysts with Cu/Sn atomic ratio close to 1:2 shows a FE of 99% toward formic acid with a high partial current density of ∼26 mA/cm^2. Density functional theory calculations further revealed the origin of the high selectivity of CuSn catalysts. It was found that OCHO* intermediate formation is more energetically favorable than COOH* on Sn sites, while it is moderate on Cu sites. The synergetic effect between Cu and Sn toward HCOOH formation was also confirmed. The current study provides significant guidance for achieving efficient CO_2 electroreduction to formic acid.

ASSOCIATED CONTENT

Supporting Information

The Supporting Information is available free of charge at https://pubs.acs.org/doi/10.1021/acsami.0c08964.

Experimental details, additional STEM images, Raman spectra, XPS data, electrochemical tests, and DFT calculation results (PDF)

https://dx.doi.org/10.1021/acsami.0c08964
ACS Appl. Mater. Interfaces 2020, 12, 41223−41229

AUTHOR INFORMATION

Corresponding Authors

Boris I. Yakobson − *Department of Chemistry, Department of Materials Science and NanoEngineering, and Smalley-Curl Institute and NanoCarbon Center, Rice University, Houston, Texas 77005, United States*; Email: biy@rice.edu

Yan Yao − *Department of Electrical and Computer Engineering and Texas Center for Superconductivity, University of Houston, Houston, Texas 77204, United States*; orcid.org/0000-0002-8785-5030; Email: yyao4@uh.edu

James M. Tour − *Department of Chemistry, Department of Materials Science and NanoEngineering, and Smalley-Curl Institute and NanoCarbon Center, Rice University, Houston, Texas 77005, United States*; orcid.org/0000-0002-8479-9328; Email: tour@rice.edu

Authors

Muqing Ren − *Department of Chemistry, Rice University, Houston, Texas 77005, United States*; orcid.org/0000-0003-1685-3764

Hongzhi Zheng − *Department of Electrical and Computer Engineering and Texas Center for Superconductivity, University of Houston, Houston, Texas 77204, United States*

Jincheng Lei − *Department of Materials Science and NanoEngineering, Rice University, Houston, Texas 77005, United States*; orcid.org/0000-0002-2459-6297

Jibo Zhang − *Department of Electrical and Computer Engineering and Texas Center for Superconductivity, University of Houston, Houston, Texas 77204, United States*; orcid.org/0000-0002-9966-8195

Xiaojun Wang − *Department of Electrical and Computer Engineering and Texas Center for Superconductivity, University of Houston, Houston, Texas 77204, United States*

Complete contact information is available at: https://pubs.acs.org/10.1021/acsami.0c08964

Author Contributions

⊥M.R., H.Z., and J.L. contributed equally to this work.

Notes

The authors declare the following competing financial interest(s): Rice University owns intellectual property (IP) on the LIG process. The IP is being licensed to a company in which none of the authors are officers or directors, but J. M. T. is a stockholder. All potential conflicts are disclosed to and managed by the Rice University Office of Sponsored Projects and Research Compliance.

ACKNOWLEDGMENTS

This work was partially funded by the Air Force Office of Scientific Research (FA9550-19-1-0296). We gratefully acknowledge the support of Universal Laser Systems for their generously providing the XLS10MWH laser system with Multiwave Hybrid technology that was used for this research. The staff of Universal Laser Systems kindly provided regular helpful advice. Density functional theory calculations were done on Rice NOTS cluster and NERSC Cori supercomputer; J.L. and B.I.Y. thank the National Science Foundation (CBET-1605848) for support.

REFERENCES

(1) Scholten, F.; Sinev, I.; Bernal, M.; Roldan Cuenya, B. Plasma-Modified Dendritic Cu Catalyst for CO_2 Electroreduction. *ACS Catal.* **2019**, *9*, 5496−5502.

(2) Tu, W.; Zhou, Y.; Zou, Z. Photocatalytic Conversion of CO_2 into Renewable Hydrocarbon Fuels: State-of-the-Art Accomplishment, Challenges, and Prospects. *Adv. Mater.* **2014**, *26*, 4607−4626.

(3) Zhang, W.; Hu, Y.; Ma, L.; Zhu, G.; Wang, Y.; Xue, X.; Chen, R.; Yang, S.; Jin, Z. Progress and Perspective of Electrocatalytic CO_2 Reduction for Renewable Carbonaceous Fuels and Chemicals. *Adv. Sci.* **2018**, *5*, 1700275−1700299.

(4) Sun, Z.; Ma, T.; Tao, H.; Fan, Q.; Han, B. Fundamentals and Challenges of Electrochemical CO_2 Reduction Using Two-Dimensional Materials. *Chem.* **2017**, *3*, 560−587.

(5) Wu, J.; Huang, Y.; Ye, W.; Li, Y. CO_2 Reduction: From the Electrochemical to Photochemical Approach. *Adv. Sci.* **2017**, *4*, 1700194−1700223.

(6) Álvarez, A.; Bansode, A.; Urakawa, A.; Bavykina, A. V.; Wezendonk, T. A.; Makkee, M.; Gascon, J.; Kapteijn, F. Challenges in the Greener Production of Formates/Formic Acid, Methanol, and DME by Heterogeneously Catalyzed CO_2 Hydrogenation Processes. *Chem. Rev.* **2017**, *117*, 9804−9838.

(7) White, J. L.; Baruch, M. F.; Pander, J. E.; Hu, Y.; Fortmeyer, I. C.; Park, J. E.; Zhang, T.; Liao, K.; Gu, J.; Yan, Y.; Shaw, T. W.; Abelev, E.; Bocarsly, A. B. Light-Driven Heterogeneous Reduction of Carbon Dioxide: Photocatalysts and Photoelectrodes. *Chem. Rev.* **2015**, *115*, 12888−12935.

(8) Larrazábal, G. O.; Martín, A. J.; Pérez-Ramírez, J. Building Blocks for High Performance in Electrocatalytic CO_2 Reduction: Materials, Optimization Strategies, and Device Engineering. *J. Phys. Chem. Lett.* **2017**, *8*, 3933−3944.

(9) Kortlever, R.; Shen, J.; Schouten, K. J. P.; Calle-Vallejo, F.; Koper, M. T. M. Catalysts and Reaction Pathways for the Electrochemical Reduction of Carbon Dioxide. *J. Phys. Chem. Lett.* **2015**, *6*, 4073−4082.

(10) Back, S.; Yeom, M. S.; Jung, Y. Active Sites of Au and Ag Nanoparticle Catalysts for CO_2 Electroreduction to CO. *ACS Catal.* **2015**, *5*, 5089−5096.

(11) Kim, C.; Jeon, H. S.; Eom, T.; Jee, M. S.; Kim, H.; Friend, C. M.; Min, B. K.; Hwang, Y. J. Achieving Selective and Efficient Electrocatalytic Activity for CO_2 Reduction Using Immobilized Silver Nanoparticles. *J. Am. Chem. Soc.* **2015**, *137*, 13844−13850.

(12) Gao, D.; Zhou, H.; Wang, J.; Miao, S.; Yang, F.; Wang, G.; Wang, J.; Bao, X. Size-Dependent Electrocatalytic Reduction of CO_2 over Pd Nanoparticles. *J. Am. Chem. Soc.* **2015**, *137*, 4288−4291.

(13) Peng, X.; Karakalos, S. G.; Mustain, W. E. Preferentially Oriented Ag Nanocrystals with Extremely High Activity and Faradaic Efficiency for CO_2 Electrochemical Reduction to CO. *ACS Appl. Mater. Interfaces* **2018**, *10*, 1734−1742.

(14) Yin, Z.; Palmore, G. T. R.; Sun, S. Electrochemical Reduction of CO_2 Catalyzed by Metal Nanocatalysts. *Trends Chem.* **2019**, *1*, 739−750.

(15) Kortlever, R.; Peters, I.; Koper, S.; Koper, M. T. M. Electrochemical CO_2 Reduction to Formic Acid at Low Overpotential and with High Faradaic Efficiency on Carbon-Supported Bimetallic Pd-Pt Nanoparticles. *ACS Catal.* **2015**, *5*, 3916−3923.

(16) Prakash, G. K. S.; Viva, F. A.; Olah, G. A. Electrochemical reduction of CO_2 over Sn-Nafion coated electrode for a fuel-cell-like device. *J. Power Sources* **2013**, *223*, 68−73.

(17) Raciti, D.; Livi, K. J.; Wang, C. Highly Dense Cu Nanowires for Low-Overpotential CO_2 Reduction. *Nano Lett.* **2015**, *15*, 6829−6835.

(18) Li, Y.; Wang, W.-N.; Zhan, Z.; Woo, M.-H.; Wu, C.-Y.; Biswas, P. Photocatalytic Reduction of CO_2 with H_2O on Mesoporous Silica Supported Cu/TiO_2 Catalysts. *Appl. Catal., B* **2010**, *100*, 386−392.

(19) Li, Q.; Fu, J.; Zhu, W.; Chen, Z.; Shen, B.; Wu, L.; Xi, Z.; Wang, T.; Lu, G.; Zhu, J.-j.; Sun, S. Tuning Sn-Catalysis for Electrochemical Reduction of CO_2 to CO via the Core/Shell Cu/SnO_2 Structure. *J. Am. Chem. Soc.* **2017**, *139*, 4290−4293.

(20) Singh, M. R.; Kwon, Y.; Lum, Y.; Ager, J. W.; Bell, A. T. Hydrolysis of Electrolyte Cations Enhances the Electrochemical Reduction of CO_2 over Ag and Cu. *J. Am. Chem. Soc.* **2016**, *138*, 13006−13012.
(21) Park, S.-M.; Razzaq, A.; Park, Y. H.; Sorcar, S.; Park, Y.; Grimes, C. A.; In, S.-I. Hybrid Cu_xO−TiO_2 Heterostructured Composites for Photocatalytic CO_2 Reduction into Methane Using Solar Irradiation: Sunlight into Fuel. *ACS Omega* **2016**, *1*, 868−875.
(22) Weng, Z.; Jiang, J.; Wu, Y.; Wu, Z.; Guo, X.; Materna, K. L.; Liu, W.; Batista, V. S.; Brudvig, G. W.; Wang, H. Electrochemical CO_2 Reduction to Hydrocarbons on a Heterogeneous Molecular Cu Catalyst in Aqueous Solution. *J. Am. Chem. Soc.* **2016**, *138*, 8076−8079.
(23) Chu, S.; Hong, S.; Masa, J.; Li, X.; Sun, Z. Synergistic Catalysis of CuO/In_2O_3 Composites for Highly Selective Electrochemical CO_2 Reduction to CO. *Chem. Commun.* **2019**, *55*, 12380−12383.
(24) Li, Y.; Chu, S.; Shen, H.; Xia, Q.; Robertson, A. W.; Masa, J.; Siddiqui, U.; Sun, Z. Achieving Highly Selective Electrocatalytic CO_2 Reduction by Tuning CuO-Sb_2O_3 Nanocomposites. *ACS Sustainable Chem. Eng.* **2020**, *8*, 4948−4954.
(25) Zheng, X.; Ji, Y.; Tang, J.; Wang, J.; Liu, B.; Steinrück, H.-G.; Lim, K.; Li, Y.; Toney, M. F.; Chan, K.; Cui, Y. Theory-Guided Sn/Cu Alloying for Efficient CO_2 Electroreduction at low Overpotentials. *Nat. Catal.* **2019**, *2*, 55−61.
(26) Li, C. W.; Kanan, M. W. CO_2 Reduction at Low Overpotential on Cu Electrodes Resulting from the Reduction of Thick Cu_2O Films. *J. Am. Chem. Soc.* **2012**, *134*, 7231−7234.
(27) Rasul, S.; Anjum, D. H.; Jedidi, A.; Minenkov, Y.; Cavallo, L.; Takanabe, K. A Highly Selective Copper-Indium Bimetallic Electrocatalyst for the Electrochemical Reduction of Aqueous CO_2 to CO. *Angew. Chem.* **2015**, *127*, 2174−2178.
(28) Xu, H.; Ouyang, S.; Liu, L.; Wang, D.; Kako, T.; Ye, J. Porous-Structured Cu_2O/TiO_2 Nanojunction Material Toward Efficient CO_2 Photoreduction. *Nanotechnol.* **2014**, *25*, No. 165402.
(29) Sarfraz, S.; Garcia-Esparza, A. T.; Jedidi, A.; Cavallo, L.; Takanabe, K. Cu-Sn Bimetallic Catalyst for Selective Aqueous Electroreduction of CO_2 to CO. *ACS Catal.* **2016**, *6*, 2842−2851.
(30) Morimoto, M.; Takatsuji, Y.; Yamasaki, R.; Hashimoto, H.; Nakata, I.; Sakakura, T.; Haruyama, T. Electrodeposited Cu-Sn Alloy for Electrochemical CO_2 Reduction to CO/$HCOO^-$. *Electrocatalysis* **2018**, *9*, 323−332.
(31) Ren, M.; Zhang, J.; Tour, J. M. Laser-Induced Graphene Hybrid Catalysts for Rechargeable Zn-Air Batteries. *ACS Appl. Energy Mater.* **2019**, *2*, 1460−1468.
(32) Ren, M.; Zhang, J.; Fan, M.; Ajayan, P. M.; Tour, J. M. Li-Breathing Air Batteries Catalyzed by MnNiFe/Laser-Induced Graphene Catalysts. *Adv. Mater. Interfaces* **2019**, *6*, No. 1901035.
(33) Zhang, J.; Ren, M.; Li, Y.; Tour, J. M. In Situ Synthesis of Efficient Water Oxidation Catalysts in Laser-Induced Graphene. *ACS Energy Lett.* **2018**, *3*, 677−683.
(34) Ye, R.; Tour, J. M. Graphene at Fifteen. *ACS Nano* **2019**, *13*, 10872−10878.
(35) Ye, R.; James, D. K.; Tour, J. M. Laser-Induced Graphene: From Discovery to Translation. *Adv. Mater.* **2019**, *31*, No. 1803621.
(36) Dimiev, A. M.; Tour, J. M. Mechanism of Graphene Oxide Formation. *ACS Nano* **2014**, *8*, 3060−3068.
(37) Ansell, R. O. X-Ray Photoelectron Spectroscopic Studies of Tin Electrodes after Polarization in Sodium Hydroxide Solution. *J. Electrochem. Soc.* **1977**, *124*, 1360−1365.
(38) Matsui, T.; Okanishi, T.; Fujiwara, K.; Tsutsui, K.; Kikuchi, R.; Takeguchi, T.; Eguchi, K. Effect of Reduction−Oxidation Treatment on the Catalytic Activity Over Tin Oxide Supported Platinum Catalysts. *Sci. Technol. Adv. Mater.* **2006**, *7*, 524−530.
(39) Zhang, J.; Zhang, C.; Sha, J.; Fei, H.; Li, Y.; Tour, J. M. Efficient Water-Splitting Electrodes Based on Laser-Induced Graphene. *ACS Appl. Mater. Interfaces* **2017**, *9*, 26840−26847.
(40) Feaster, J. T.; Shi, C.; Cave, E. R.; Hatsukade, T.; Abram, D. N.; Kuhl, K. P.; Hahn, C.; Nørskov, J. K.; Jaramillo, T. F. Understanding Selectivity for the Electrochemical Reduction of Carbon Dioxide to Formic Acid and Carbon Monoxide on Metal Electrodes. *ACS Catal.* **2017**, *7*, 4822−4827.
(41) Kaneco, S.; Hiei, N.-h.; Xing, Y.; Katsumata, H.; Ohnishi, H.; Suzuki, T.; Ohta, K. High-Efficiency Electrochemical CO_2-to-Methane Reduction Method Using Aqueous $KHCO_3$ Media at Less Than 273 K. *J. Solid State Electrochem.* **2003**, *7*, 152−156.
(42) Kauffman, D. R.; Thakkar, J.; Siva, R.; Matranga, C.; Ohodnicki, P. R.; Zeng, C.; Jin, R. Efficient Electrochemical CO_2 Conversion Powered by Renewable Energy. *ACS Appl. Mater. Interfaces* **2015**, *7*, 15626−15632.
(43) Wang, J.; Ji, Y.; Shao, Q.; Yin, R.; Guo, J.; Li, Y.; Huang, X. Phase and Structure Modulating of Bimetallic CuSn Nanowires Boosts Electrocatalytic Conversion of CO_2. *Nano Energy* **2019**, *59*, 138−145.
(44) Peterson, A. A.; Abild-Pedersen, F.; Studt, F.; Rossmeisl, J.; Nørskov, J. K. How copper Catalyzes the Electroreduction of Carbon Dioxide into Hydrocarbon Fuels. *Energy Environ. Sci.* **2010**, *3*, 1311−1315.
(45) Karamad, M.; Hansen, H. A.; Rossmeisl, J.; Nørskov, J. K. Mechanistic Pathway in the Electrochemical Reduction of CO_2 on RuO_2. *ACS Catal.* **2015**, *5*, 4075−4081.
(46) Jiang, B.; Zhang, X.-G.; Jiang, K.; Wu, D.-Y.; Cai, W.-B. Boosting Formate Production in Electrocatalytic CO_2 Reduction over Wide Potential Window on Pd Surfaces. *J. Am. Chem. Soc.* **2018**, *140*, 2880−2889.
(47) Klinkova, A.; De Luna, P.; Dinh, C.-T.; Voznyy, O.; Larin, E. M.; Kumacheva, E.; Sargent, E. H. Rational Design of Efficient Palladium Catalysts for Electroreduction of Carbon Dioxide to Formate. *ACS Catal.* **2016**, *6*, 8115−8120.

https://dx.doi.org/10.1021/acsami.0c08964
ACS Appl. Mater. Interfaces 2020, 12, 41223−41229